The International Journal of Advanced Manufacturing Technology (2019) 103:1769–1780
https://doi.org/10.1007/s00170-019-03545-0

ORIGINAL ARTICLE

# Effect of scanning strategy and speed on the microstructure and mechanical properties of selective laser melted IN718 nickel-based superalloy

Mostafa Amirjan [1] · Hassan Sakiani [2]

Received: 12 July 2018 / Accepted: 4 March 2019 / Published online: 11 April 2019


**Abstract**
In the present study, the properties of selective laser melted IN718 superalloy specimens, prepared by using different processing parameters, were investigated. The scanning strategy (island strategy with and without 30° interlayer rotation and continuous bi-directional scanning with and without 90° interlayer rotation) and scanning speeds of 500, 700, and 1000 mm/s were selected as variables to prepare the superalloy samples. Then, the microstructure and mechanical properties (hardness and compressive strength) were characterized. The results showed, in a given scanning strategy, the density decreases as the scanning speed increases. Also, the island strategy with interlayer rotation during fabrication process leads to a higher level of density (near full density, about 8.20 g/cm3). Interlayer rotation resulted in a more uniform structure by re-melting of deposit layers in different directions during deposition of next layers in both scanning strategies. The higher values of hardness and compressive yield strength were obtained from the samples produced using continuous scanning strategy. Among the investigated samples, the sample produced with continuous scanning strategy with 90° interlayer rotation, 500 mm/s scanning speed has the highest value of hardness, 330 Vickers, and compressive yield strength, 686 MPa.

**Keywords** Selective laser melting (SLM) · IN718 superalloy · Scanning strategy · Scanning speed

## 1 Introduction

The combination of excellent mechanical properties and corrosion resistance of IN718 (Ni-Cr-Fe) austenitic superalloy makes it a good candidate for a gas turbine, aerospace jet engine and blades, and some other high-temperature applications [1, 2]. There are several conventional methods for manufacturing of IN718 parts such as casting and forging. Besides the need for huge investment of these processes (equipment and tools), there are geometry restrictions (i.e., hollow and complex sections) which limit the manufacturing of very complex features. Additive manufacturing processes are the techniques which give the flexibility and materials freedom for production of the complex parts layer by layer [3, 4]. These techniques create the parts directly without using tools. Selective laser melting (SLM) of metals is an additive manufacturing powder bed process in which a certain powder is applied layer by layer on a platform and a laser beam selectively melts the powder layer according to predefined layer design. There are several processing parameters such as laser power and focus diameter of the laser beam, layer thickness, and hatch spacing that affect the final product quality and properties [3–5]. The production of an intact part with good properties needs the appropriate selection of processing parameters.

In recent years, some researchers have investigated the manufacturing and characterization of IN718 superalloys prepared by the SLM technique [1–10]. Trosch et al. [1], in their research, studied and compared the IN718 superalloy part's properties, manufactured by casting, forging, and SLM processes. The SLM samples were prepared in three different orientations of horizontal, vertical, and 45°. They found that the average tensile strength of SLM samples is higher than conventionally manufactured ones. Also, the strength of samples in 45° direction is higher than other orientations. Jia and Gu [2] have investigated the densification and properties of

✉ Mostafa Amirjan
mamirjan@nri.ac.ir

[1] Metallurgy Division, Department of Chemical and Materials Engineering, Niroo Research Institute (NRI), Tehran 1468617151, Iran

[2] Faculty of mining and metallurgy, Amirkabir University of Technology, Tehran 158754413, Iran

**Table 1** Chemical composition of IN718 powder

| Elements | Cr | Fe | Nb + Ta | Mo | Ti | Al | Si | Ni |
|---|---|---|---|---|---|---|---|---|
| wt.% | 19.3 | 16.84 | 4.66 | 4.57 | 0.59 | 0.55 | 0.06 | 53.43 |

SLM prepared samples using different laser energies and scanning speeds. The results showed that the laser energy density is a key factor for densification. Valdez et al. [3] studied the effect of porosity levels on the mechanical properties of IN718 SLM samples. They realized that the compression behavior of samples with lower density (higher porosity level) is similar to open cell foam and as the density increased, the bulk metallic behavior was observed. Xia et al. [4] have simulated the porosity evolution and scanning speed effects on the porosity levels during the SLM process. They found that, as the scanning speed increases, the type of porosity changes from metallurgical one to open porosity on the top surface. This phenomena leads to weak metallurgical bonding properties of interlayer interfaces. In research done by Tucho et al. [5], the microstructure and hardness of as-printed and heat-treated IN718 SLM samples manufactured in vertical and horizontal directions were investigated. They realized that despite other reports, the as-printed samples have the non-columnar grain microstructures. Also, the vertically manufactured samples indicated 13% higher hardness values than horizontal ones. In Deng et al. [6] research, the IN718 superalloy produced by SLM was characterized by the microstructure and the dependence of sample orientation on the mechanical properties. They observed that there is a difference between the properties of vertically and horizontally built samples due to crystallographic features, the amount of residual stress, and dislocations. Caiazzo et al. [7] investigated the SLMed cylindrical samples of IN718 prepared in three different orientations to

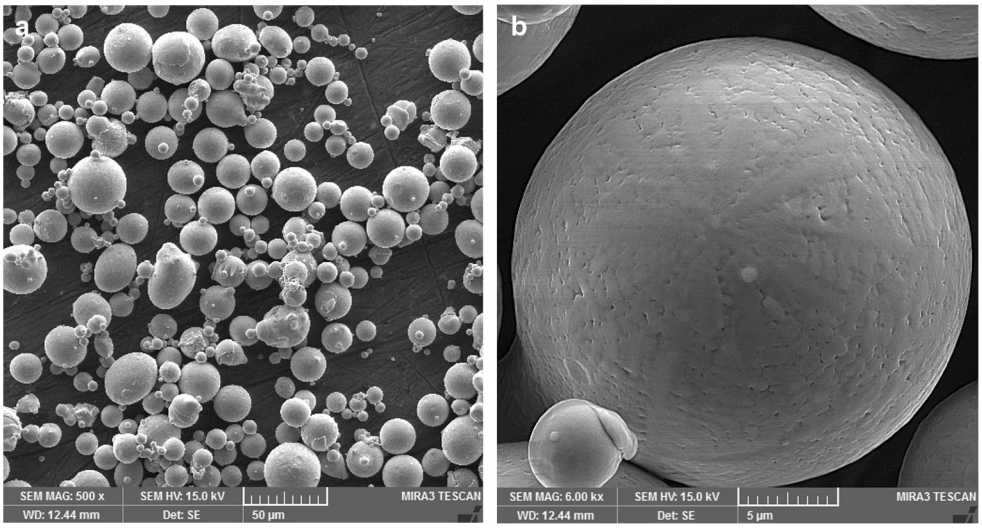


**Fig. 1** a morphology and size distribution of particles

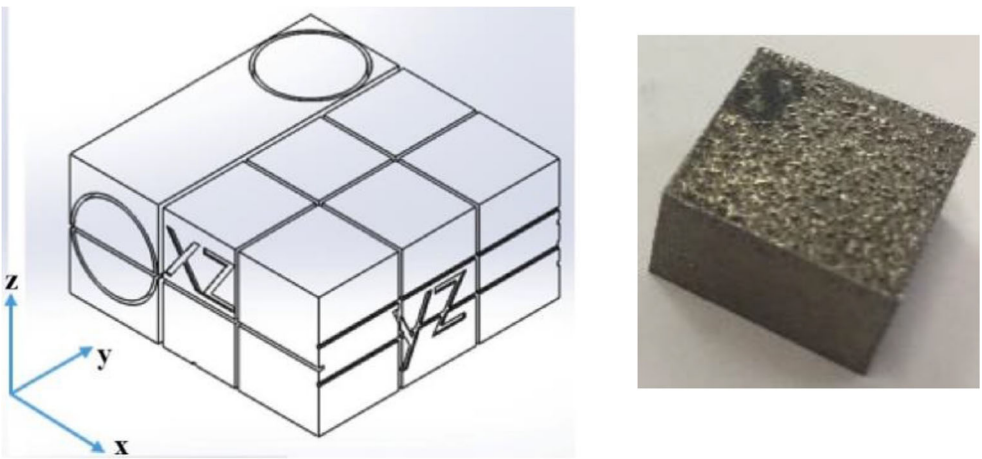


**Fig. 2** The schematic and as-fabricated sample

**Table 2** The specification of prepared samples

| Sample designation | Strategy | | Scanning speed (mm/s) |
|---|---|---|---|
| | Scanning strategy | Interlayer rotation (°) | |
| I-S500-R30 | Island | 30 | 500 |
| I-S700-R30 | Island | 30 | 700 |
| I-S1000-R30 | Island | 30 | 1000 |
| I-S1000-R0 | Island | 0 | 1000 |
| I-S500-R0 | Island | 0 | 500 |
| C-S500-R90 | Continuous | 90 | 500 |
| C-S700-R90 | Continuous | 90 | 700 |
| C-S1000-R90 | Continuous | 90 | 1000 |
| C-S1000-R0 | Continuous | 0 | 1000 |
| C-S500-R0 | Continuous | 0 | 500 |

build direction (0°, 45°, 90°) using raster strategy with 67° interlayer rotation. A negligible anisotropy in mechanical properties was found. A 3D finite element modeling was utilized to investigate the effect of different scanning strategy on the IN718 part temperature, deformation, and residual stress by Cheng et al. [8]. The results showed that the 45° inclined line scanning has a smaller build direction deformation and reduced residual stress among the investigated samples. Wang et al. [9] investigated the microstructure and mechanical properties of IN718 sample prepared by SLM technique using the scanning strategy of bi-directional hatch of layers with 90° interlayer rotation at the constant scanning speed of 25 m/min. They understood the dependency of mechanical properties to microstructure and its relation to grain structure, the type, and shape of precipitates in microstructure before and after heat treatment. In a work by Choi et al. [10], the densification and microstructure of selective laser melting products of IN718 superalloy prepared using a variation of laser scanning speed with a constant continuous scanning strategy were studied. The scanning speed showed a crucial role in the density and properties of samples so that it affects the melt pool features, solidification, and, as a result, microstructure and final properties.

As it can be seen from several researches, the scanning speed, scanning strategy, laser power, hatch spacing/overlapping, and interlayer rotations are the key factors in the manufacturing process and final properties. The related researches often have considered the heat treatment and final properties of SLMed IN718 superalloy and there are a few studies about the investigation of processing parameters such as scanning strategy and speed on the as-fabricated microstructure and properties. Also, the interlayer rotation in scanning strategy, which affects the interlayer bonding and microstructure evolutions, just has been reported for 90° or 45°.

As a systematic study, in the present research, the microstructure and mechanical properties (including hardness and compressive yield strength) of as-printed SLMed IN718 samples were studied. The scanning strategy (island and continuous strategy) and scanning speed were investigated as processing variables. In order to examine the effect of the interlayer rotation of scanning strategy on consolidation and microstructure, a higher level of rotation (i.e., 30°) was utilized for island strategy besides the interlayer rotation of 90° for continuous one. Laser spot diameter and power, also hatch spacing, were kept constant in the processing of samples.

## 2 Experimental

Gas-atomized IN718 powder (D10 (17 μm), D50 (35 μm), D90 (52 μm)) with a chemical composition according to Table 1 is used in the present work. Powder particles size and morphology are shown in Fig. 1.

**Table 3** Density and porosity values of as-printed samples

| Sample | Porosity (%) | Density (g/cm$^3$) |
|---|---|---|
| I-S500-R30 | 0.10 | 8.20 |
| I-S700-R30 | 0.10 | 8.15 |
| I-S1000-R30 | 0.25 | 7.95 |
| I-S1000-R0 | 1.00 | 8.07 |
| I-S500-R0 | 0.21 | 8.11 |
| C-S500-R90 | 0.30 | 8.10 |
| C-S700-R90 | 1.70 | 8.05 |
| C-S1000-R90 | 5.70 | 8.00 |
| C-S1000-R0 | 4.40 | 7.95 |
| C-S500-R0 | 1.62 | 7.98 |

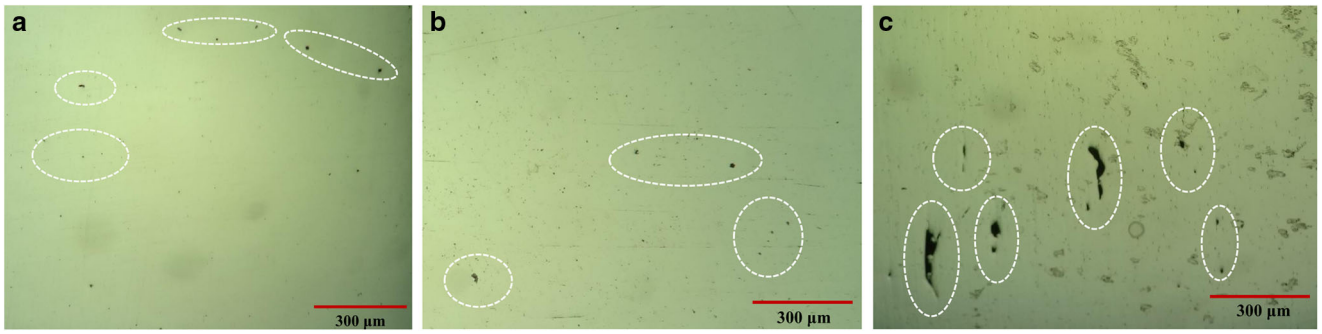


**Fig. 3** Optical micrograph of samples **a** "I-S500-R30," **b** "I-S700-R30," and **c** "I-S1000-R30"

A laboratory scale SLM metal printing machine (Noura-M100) equipped with a Yb-fiber laser source with the power of 200 W power was used for fabricating samples along the *z* direction. In order to investigate the scanning strategy and speed on the microstructure and properties, the power of 170 W and 80-µm laser spot diameter and layer thickness of 30 µm was chosen as constant parameters for sample preparation. Considering 30% overlap between laser tracks, hatch spacing was calculated to be 56 µm. The samples (dimension of $15 \times 15 \times 10$ mm$^3$) were prepared by 4 different scanning strategies including the following:

- Random island scanning with $5 \times 5$ mm$^2$ islands (zigzag scanning of each island) with and without 30° interlayer rotation, (for each subsequent layer, the island pattern shifted by 1 mm in both *x* and *y* directions) and
- Continuous bi-directional scanning with and without 90° interlayer rotation

Note that it was considered two factors to choose island dimension; first, same preparation procedure according to sample dimension and more available island interfaces for investigation and possibly finer microstructure. Also, three

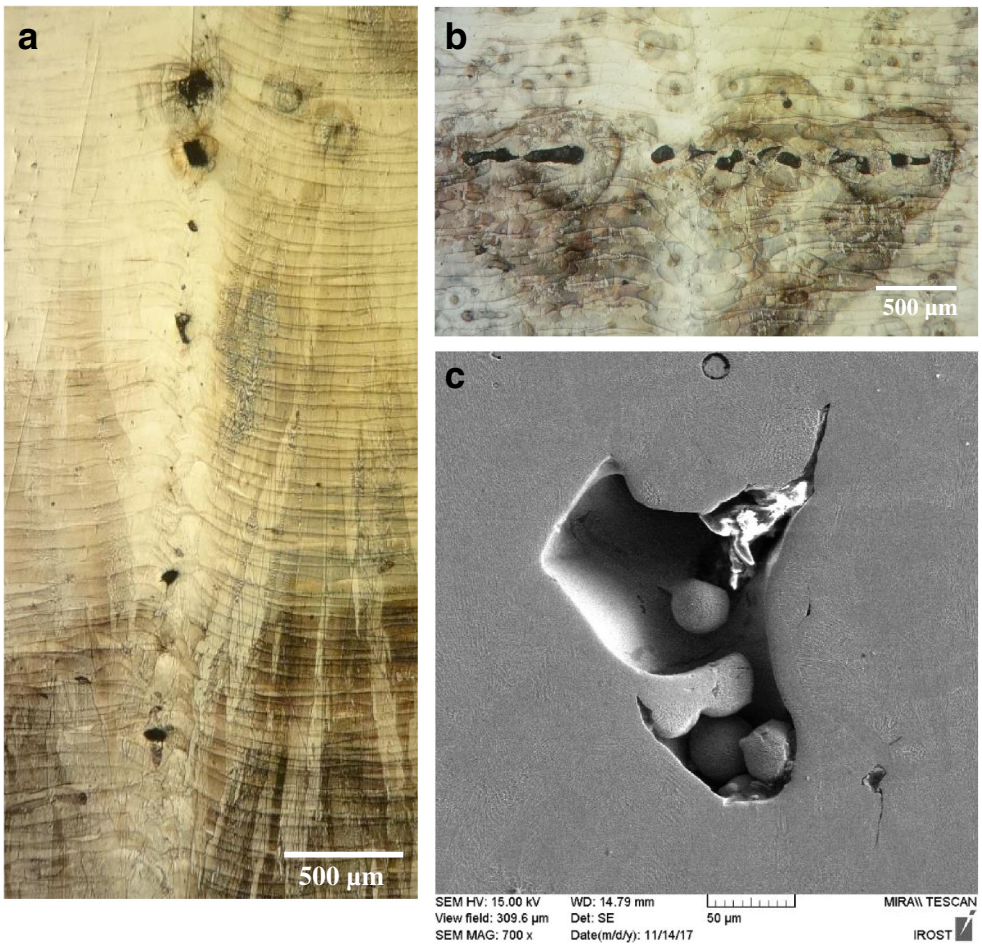


**Fig. 4** Array of porosity in sample "I-S1000-R0" **a** yz plane, **b** xy plane, **c** SEM micrograph of a lack of fusion pore in an array of pores formed in the xz plane

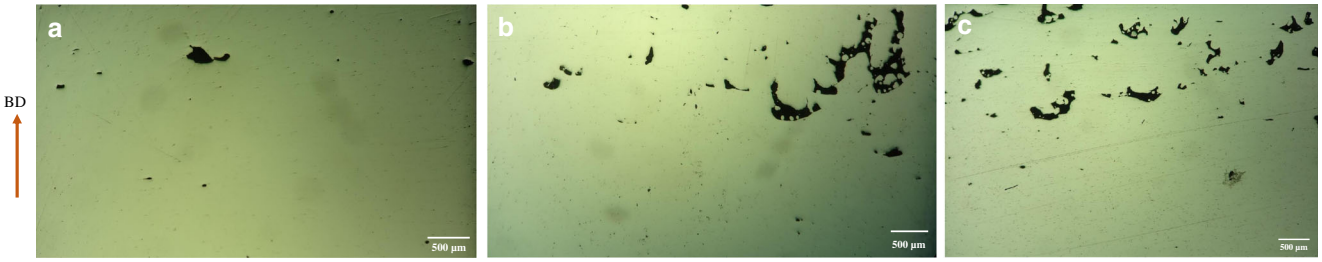


**Fig. 5** Porosity in samples produced by C strategy **a** "C-S500-R90", **b** "C-S700-R90", **c** "C-S1000-R90"

different scanning speeds (500, 700, 1000 mm/s) were used as variable parameters. The argon flow rate of about 3–4 l/min was utilized inside the evacuated build chamber to avoid contamination and oxygen content less than 0.4 ppm, during the building process. The same processing parameters were used to prepare the upper surface layers. To avoid undesirable porosity of the upper layers, the thickness of 0.5 mm was removed from the samples' surface. Figure 2 shows the schematic and an as-fabricated sample. The specification of prepared samples is listed in Table 2.

The density of as-printed samples was determined based on the Archimedes principle, according to ASTM B962 standard

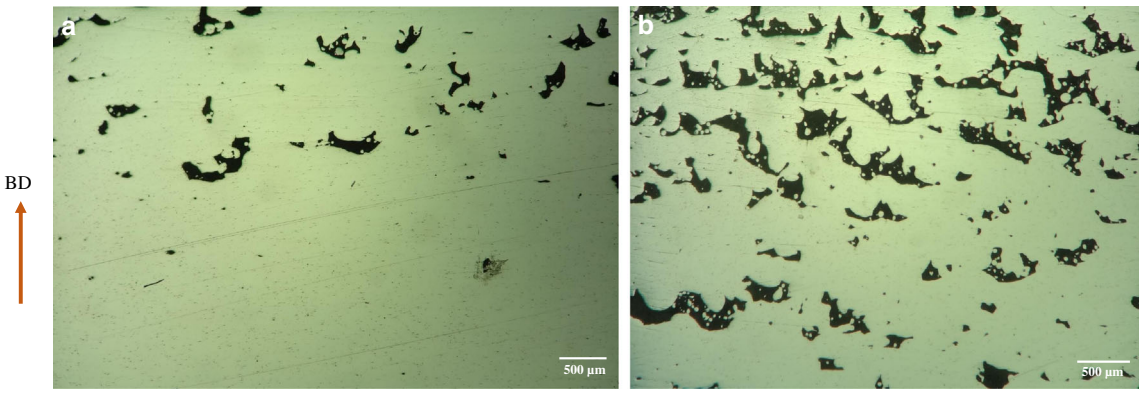


**Fig. 6** Porosity in samples produced by "C" strategy, **a** "C-S1000-R90", with interlayer rotation, **b** "C-S1000-R0" without interlayer rotation

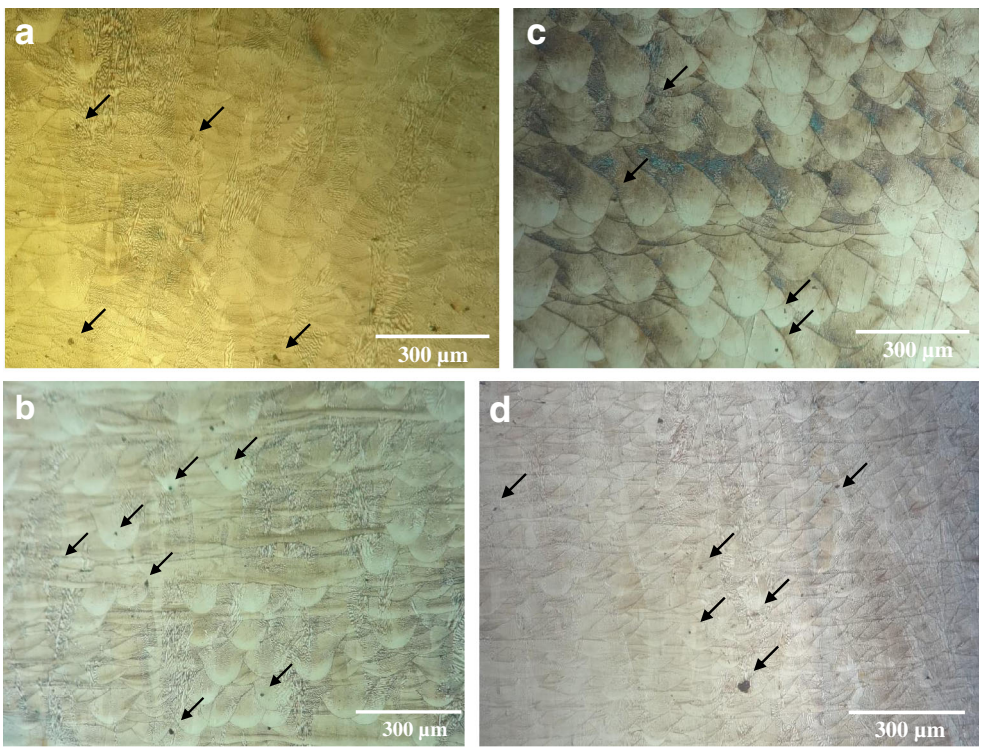


**Fig. 7** The OM microstructures from xz direction for **a** "I-S500-R30", **b** "C-S500-R90", **c** "I-S700-R30," and **d** "C-S700-R90"


**Fig. 8** The microstructure of "C-S700-R90" sample in the 3D section

[11]. Then, each sample was cut and prepared for microstructure and mechanical property investigations.

The grounded and polished samples were etched with aqua regia (solution of $HNO_3$ and HCl in 1:3 M ratio) for microstructural investigations. To quantify and study the samples' porosity, a polished xz section of each sample was captured with an optical microscope (OM) equipped with a digital camera before etching. Then, about 10–14 micrographs were used to quantify the porosity level using Clemex image analysis software. OM and field emission scanning electron microscopy equipped with energy dispersive spectroscopy (FESEM-EDS) were used to study morphology and chemical composition of phases formed in the microstructure.

The hardness of the samples was measured using a universal testing machine according to the Vickers method, applying 30 kg for 20 s.

Compression test was done on a cylindrical sample with an H/D ratio of 1:5 which was prepared from the sample block in a way that its axis was perpendicular to the building direction (BD). The strain rate of 0.005 mm/min was used in accordance with ASTM-E9 standard [12].

## 3 Results and discussion

### 3.1 Effect of scanning strategy and speed on density/porosity

The porosity of samples was quantified by calculating the relative ratio of the pore area to the surface area of the sample (average of different surfaces) as well as density measurement. Calculated densities based on the Archimedes principle and porosity percentage of the samples are listed in Table 3.

It could be suggested that in higher scanning speeds, the heat input/energy are not sufficient to obtain the fully dense sample. This issue observed for both applied scanning strategies. Two types of porosity were detected in samples: spherical gas pores and irregular shape pores of lack of fusion, which both of them were also reported by other researchers [13].

In island strategy, increasing the scanning speed up to 700 mm/s do not significantly affect porosity and density of the samples and only a few small gas pores (smaller than 20 μm) formed in "I-S500-R30" and "I-S700-R30" samples, which were uniformly distributed in the microstructure (Fig. 3a, b). Therefore, their densities were near the full density of IN718 (8.18–8.22 g/cm$^3$ [10, 14]). Processing with a speed of 1000 mm/s resulted in the formation of some larger irregular pores (Fig. 3c). This lack of fusion pores formed specifically near the surface of the sample.

Gas pores in the sample "I-S500-R30" are larger than "I-S700-R30." This could be reasonable because of more heat input in the former which promoted evaporation of the powder bed as a result of more peak temperature in the building process [10]. On the other hand, with an increasing scan speed up to 1000 mm/s (sample "I-S1000-R30"), reduction of heat input resulted in lower peak temperature in the melt pool. At high scanning speeds, the depth of the pool is not enough to melt the precede layers. Therefore, more viscous melt would be formed which has not enough flowability. This lack of melt flow resulted in the formation of lack of fusion pores and weak bonding of layers [2, 4, 15].

However, fabrication by island strategy without interlayer rotation (sample "I-S1000-R0") produced a relatively dense structure in each island, but arrays of lack of fusion pores formed in inter-island boundaries, as can be seen in Fig. 4 a, b, in both parallel and perpendicular planes to BD. At these zones, there was not enough heat input and melt flow as a result of next layer deposition. Figure 4 c confirmed that theses pores formed as a result of lack of fusion and melt flow because un-melted powder particles could be seen inside the pore.

**Table 4** The dimensions (width and depth) of melt pools

| Sample | Mean width of laser track (μm) | Mean depth of laser track (μm) |
|---|---|---|
| I-S500-R30 | 80.8 ± 6.75 | 41 ± 13.3 |
| I-S700-R30 | 70 ± 5.60 | – |
| I-S1000-R30 | 63.6 ± 5.50 | 33.8 ± 11 |
| I-S1000-R0 | 62.3 ± 3.35 | 31.8 ± 8.1 |
| I-S500-R0 | 86 ± 5.82 | 43 ± 9.2 |
| C-S500-R90 | 78 ± 4.30 | 91.6 ± 34 |
| C-S700-R90 | 67.6 ± 4.62 | 53 ± 19 |
| C-S1000-R90 | 64.4 ± 4.23 | 46 ± 8.1 |
| C-S1000-R0 | 64.2 ± 4.51 | 34 ± 10.4 |
| C-S500-R0 | 80 ± 5.2 | 94 ± 30 |

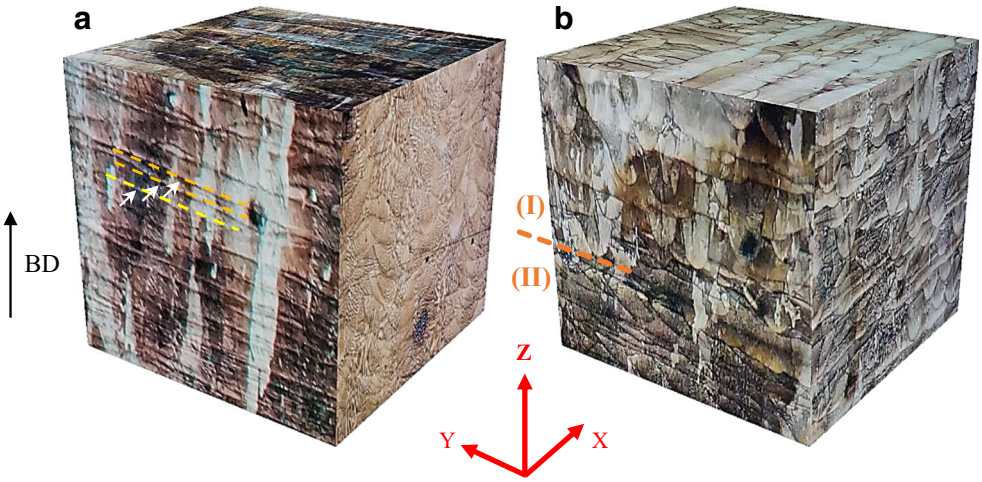


**Fig. 9** Illustrative 3D model of samples **a** "I-S500-R30" and **b** "C-S500-R90"

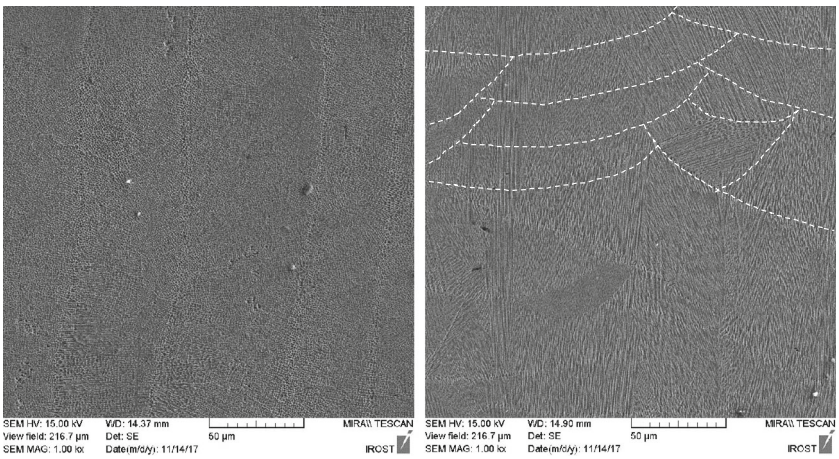


**Fig. 10** The SEM micrographs of "I-S700-R30" sample, along with build direction (right) and perpendicular to build direction (left)

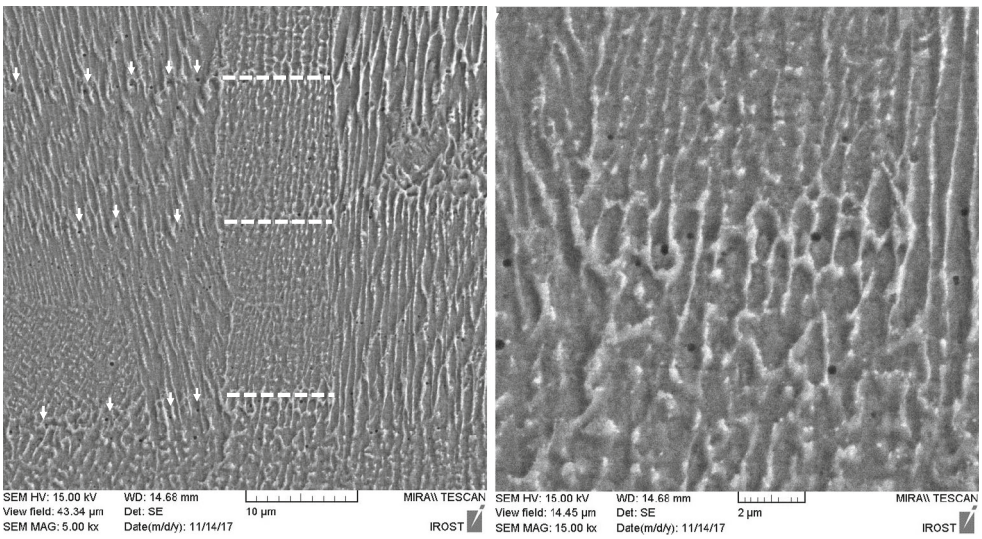


**Fig. 11** Continuous growth of columnar grains passing the boundaries of pools along build direction for "I-S700-R30" sample in yz plane, indicating the layers' interface and micro-porosities/carbides (left), and layers' interface at higher magnification (right)

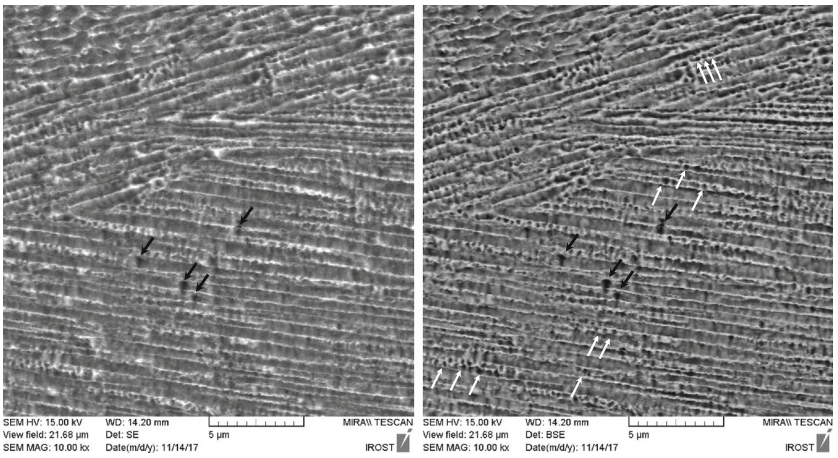


**Fig. 12** The SEM micrographs of yz plane of "I-S1000-R30" sample, indicating micro-porosities (black arrows) and carbides (white arrows), SE image (left) and BSE image (right)

Fabrication with continuous strategy obtained the samples with lower density than island strategy. In all samples, it is obvious that the lack of fusion pores for samples prepared with "C" strategy. Therefore, it seems that the scanning speeds selected near or beyond the suitable speed to produce a dense sample by this strategy. Therefore, it could be suggested that scanning with continuous pattern needs lower speeds than the island strategy. On the other hand, increasing scanning speed leads to density reduction of the printed samples in both strategies. Continuous scanning without interlayer rotation could worsen the situation as it could be seen in Fig. 5. Indeed, interlayer rotation resulted in a more uniform structure by re-melting of deposit layers in different directions during deposition of next layers. It was reported that the more interval number between re-matching directions of the melting line with an initial layer increases the probability of defect removal and anisotropy [15].

Among samples which were fabricated by continuous strategy, "C-S500-R90" has a few gas pores and inter-layer porosities which imply that the process parameters are almost suitable; however, the formation of irregular lack of fusion pores near the surface of the sample implies that lower scanning speeds might improve the integrity of the as-printed sample. The "C-S700-R90" sample has more critical conditions and more irregular shape pores formed in beneath the surface layers. The "C-S1000-R90" sample has the lowest heat input among the samples printed by continuous strategy. In this sample, interlayer pores could be seen also in the bottom layers of the sample, but they become more and larger along building direction. Porosities in layers near the top surface of the sample elongated through many layers up to a thickness more than 500 μm. The near surface portion of continuously scanned samples with interlayer rotation is shown in Fig. 6. Lack of interlayer rotation in continuous strategy worsened conditions to achieve a dense structure and caused more porosity formation in the samples illustrated in Fig. 6. These micrographs have been prepared from the surface portions of the yz plane of "C-S1000-R90" and "C-S1000-R0" samples.

Overall, using the selected processing parameters, island strategy showed the samples with higher density. This issue can be seen in the microstructures of Fig. 7 related to both strategies in different scanning speeds. Also, the interlayer rotation is a necessary requirement to achieve a dense structure free of aligned pores.

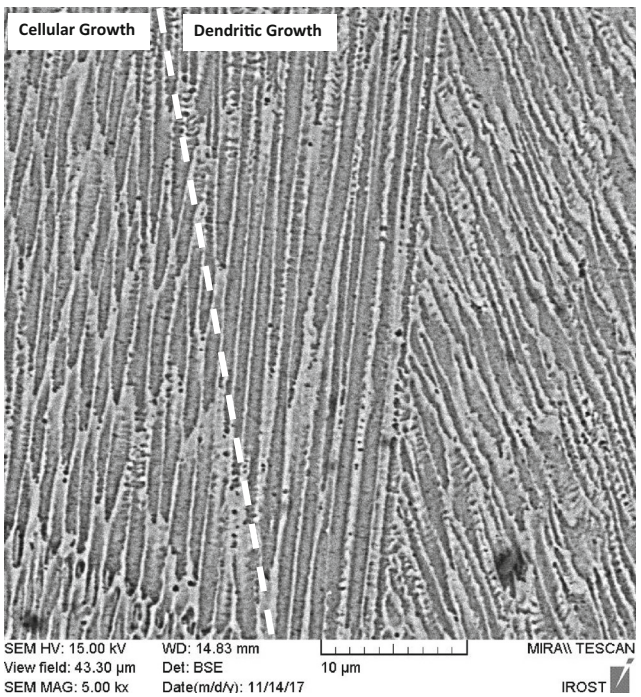


**Fig. 13** Simultaneous cellular and dendritic growth and transition region in a grain ("I-S700-R30" sample)

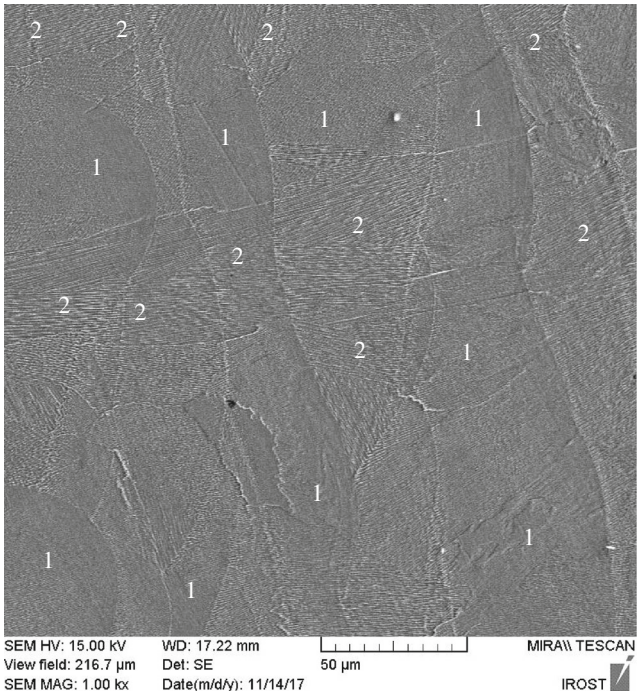


**Fig. 14** Coarse structure in pools' overlapping regions (yz plane in "C-S700-R90" sample)

## 3.2 Effect of scanning strategy and speed on the microstructure

A typical microstructure of the samples in the 3D section is shown in Fig. 8. In the section parallel to BD (xz plane) melt pools could clearly be seen and in xy plane which is perpendicular to build direction, tracks of the laser movements are obvious.

Average width and depth of melt pools in all samples were measured from etched microstructures and listed in Table 4. Width and depth of melt pools were calculated from xy and yz planes, respectively.

The depth of melt pools in the "C-S500-R90" sample is more than 2 times higher than the thickness of the layers in the "I-S500-R30" sample; however, they were fabricated by the same process parameters. The average thicknesses of the layers in island-scanned samples (~ 30–40 μm) are similar to each other, and approximately equal to the thickness of the powder bed layer (~ 30 μm). However, the depth of melt pools in continuously scanned samples dropped sharply with increasing scanning speed from 500 to 700 mm/s, and its changes became less beyond that. This trend is consistent with the trend of mechanical property changes which would be discussed in the next section. The average width of melt pools which were measured from xz plane images of the samples is nearly the same for corresponding scanning speeds in both strategies.

It could be seen that yz plane of the samples which were fabricated by island strategy is different from the ones made by continuous strategy (Fig. 9). This difference is seemed to be a result of interlayer rotation angle which caused the samples produced by island strategy (with an interval number of 12) to have layered microstructure in yz plane and melt pools were not seen anymore. However, in a continuous strategy whose interval number is 4, less uniform structure would be obtained and melt pools could be also seen on yz planes. Improvement in the uniformity of the microstructure and more isotropy in mechanical properties by increasing interval number was also reported before [16]. Indeed, in samples which were built with continuous strategy, xz and yz planes are similar to each other, but in island scanned samples, xz and yz planes have different microstructure.

In island scanned samples along BD, the microstructures are the same and similar to Fig. 9, but in the continuously scanned samples, microstructure could roughly be divided into two distinct sub-structures as could be seen in Fig. 9. At first one, melt pools are clear and in the other one, shallow

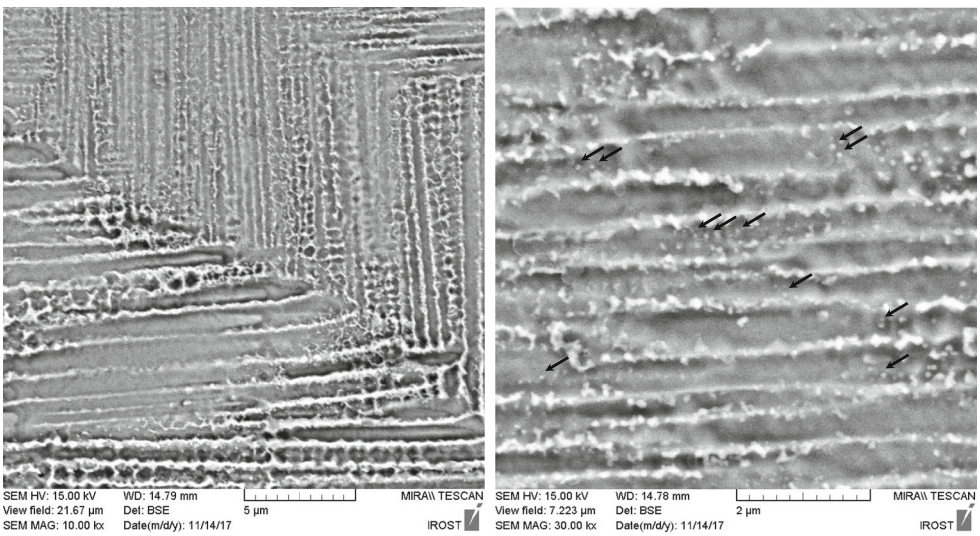


**Fig. 15** Dendritic structure (left) and the formation of secondary phase (right) (black arrows: γ′ precipitates) in inter-dendritic spaces (xz plane "I-S500-R30 sample)

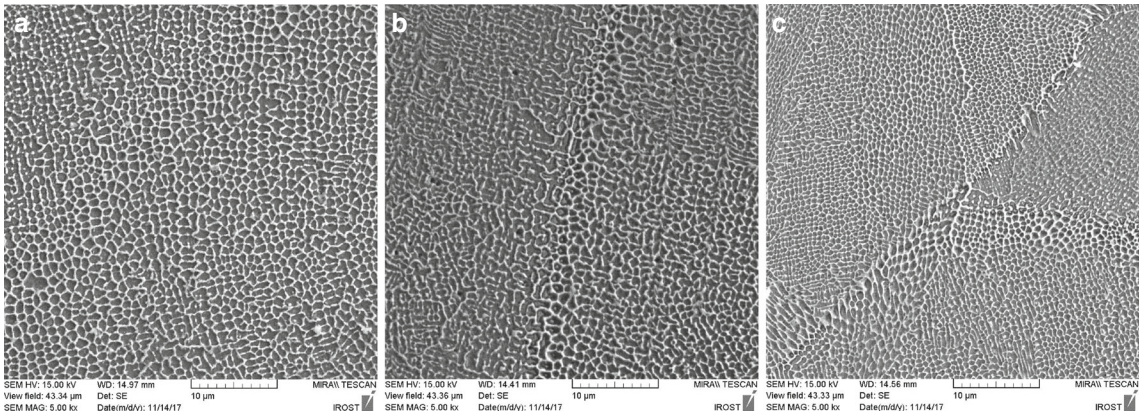


**Fig. 16** SEM micrographs of the xy plane of **a** "I-S500-R30", **b** "I-S700-R30", **c** "I-S1000-R30" samples

melt pools could be seen which elongated in a perpendicular direction to BD and parallel to the laser movement direction.

The SEM micrographs of "I-S700-R30" sample in xz and xy directions are illustrated in Fig. 10. The columnar grains oriented across the build direction can be seen in xz direction. Some grains pass the boundaries of several grains (Fig. 11). This epitaxial growth along build direction leads to the improvement of interlayers' bonds [17]. The slight deviation of some grains from building direction is attributed to laser movements [13, 18, 19].

There exists a row of spherical porosity smaller than 1 μm along the layers' interface which is indicated with arrows (Fig. 11). Chlebus et al. [20] have reported that, in SLM samples, the spherical Nb, Ti-rich carbides can be formed in inter-dendritic spaces. Their morphology indicates that these carbides were nucleated from the melt before eutectic reaction and Laves-phase formation. So, they recognized these features as the phase. Further observations of microstructure in this study showed that there exists both porosity and carbide phase in inter-dendritic spaces (Fig. 12). The arrows show the recognized porosities (black arrows) and carbide phases (white arrows).

The SEM micrograph of "I-S700-R30" sample in Fig. 13 indicates the simultaneous cellular and dendritic growth and the transition regions between them in a grain. The cell size in cellular structure and inter-dendritic distances in the dendritic structure was less than 1 μm. The effective heat flux direction determines the growth of dendrites and cells in a grain [19]. Effective heat flux derived from horizontal heat flux originates from laser movement and vertical heat flux from heat transfer to the substrate. It seems that the overlapping regions of laser tracks have a coarser microstructure than adjacent ones.

Accordingly, the pool middle regions, generally, have the finer structure than the edges of pools (Fig. 14). The fine and overlapping regions, in Fig. 14, are illustrated as "1" and "2," respectively. The coarsening of microstructure in overlapping regions is in agreement with other researches [21, 22]. It is expressed that the re-passing of the laser from the overlapping region is the reason for this phenomena. So, the cooling rate in overlapping regions is lower than adjacent regions.

Generally, the scanning speed and laser power affect the thermal gradient (G) and solidification rate (R). For predicting the grain structure (cellular/dendritic), the solidification windows can be utilized [13].

The solidification of IN718 superalloy, usually, is controlled by Nb and C. In cooling rates over than 103 K/s, it is expected that the formation of the supersaturated solid solution as matrix and some NbC carbides and Laves phases [19]. The SEM micrograph of "I-S500-R30" sample along the build direction shows some phases in inter-dendritic spaces (Fig. 15).

The Laves phases and NbC carbides are formed as a result of a eutectic reaction in inter-dendritic regions when the Nb, Mo, and C are as high as sufficient [19]. Therefore, it is observed in the last solidified region during each laser scan. The nano-metric cubic precipitates in inter-dendritic spaces of Fig. 15 (arrows) have the morphology and features of $\gamma'$ phase.

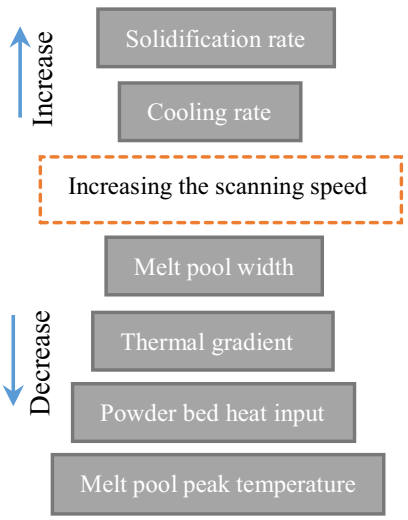


**Fig. 17** The variation of SLM process parameters with a scanning speed

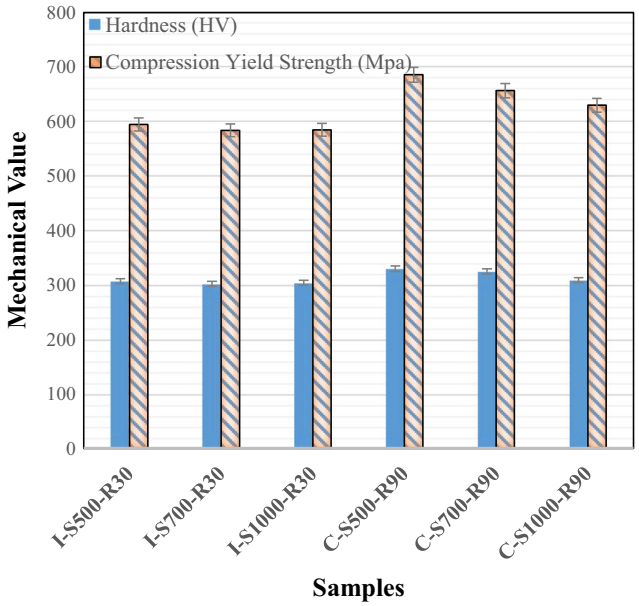


**Fig. 18** Comparison of hardness and yield strength of samples were built by the island and continuous strategy with interlayer rotation

Microstructural observations depicted that, by increasing the scanning speed which resulted in a decrease in input energy to the powder bed, the size of cells decreased. This trend is shown in Fig. 16 for xy plane of the samples which were built by island scanning with interlayer rotation. The results of increasing the scanning speed are illustrated in Fig. 17. These effects cause the formation of finer structures.

### 3.3 Effect of scanning strategy and speed on mechanical properties

Hardness and compressive yield strength of the samples are illustrated in Fig. 18. According to the results, the higher values of hardness and compressive yield strength of the samples belong to those which were built by continuous strategy. It could have a number of reasons, including (1) finer microstructure (Fig. 16), (2) formation of a higher amount of strengthening phases ($\gamma'$ and $\gamma''$) in the microstructure (Fig. 15), and (3) more residual stress and more dislocation density. According to samples microstructure, it could be suggested that in "C" (continuous) strategy, deposited layers were less affected from next layer deposition in comparison to "I" (island) strategy. Evidence of this suggestion is disappearing of the Gaussian morphology of melt pools in "I" strategy samples and formation of layered morphology in their yz plane, which was reported to be indicative of multi-pass melting with significant overlapping [22]. Layered morphology on the other hand is an evidence of slower cooling rate which could result in coarser dendrite arm spacing [22]. In Fig. 19, coarser microstructure of "I-S1000-R30" sample in comparison to "C-S1000-R90" sample is shown, as a representative example for different size of epitaxial grains and arm spacing in samples which were built by "I" and "C" strategy.

As mentioned before, different melt pool morphologies were formed in samples which were fabricated by "I" and "C" strategy; however, their process parameters (e.g., laser power, scanning speed, hatching space, powder layer thickness) were the same except the pattern of laser scanning. Different scanning patterns resulted in a different re-heating and re-melting cycles which make cooling rate, local melt flow, and local heat treatment in the heat-affected zone near the melt pool different. More re-melting and local heat treatment which occurred for depositing layers in "I" strategy would be able to relieve more residual stress in the sample to reduce its hardness and yield strength.

It seems that despite the continuous strategy, the selection of process parameters in island strategy is such a way that increasing scanning speed up to 1000 mm/s do not significantly deteriorate the mechanical properties of the sample. In continuous scanning strategy, by increasing scanning speed, porosity increased rapidly and

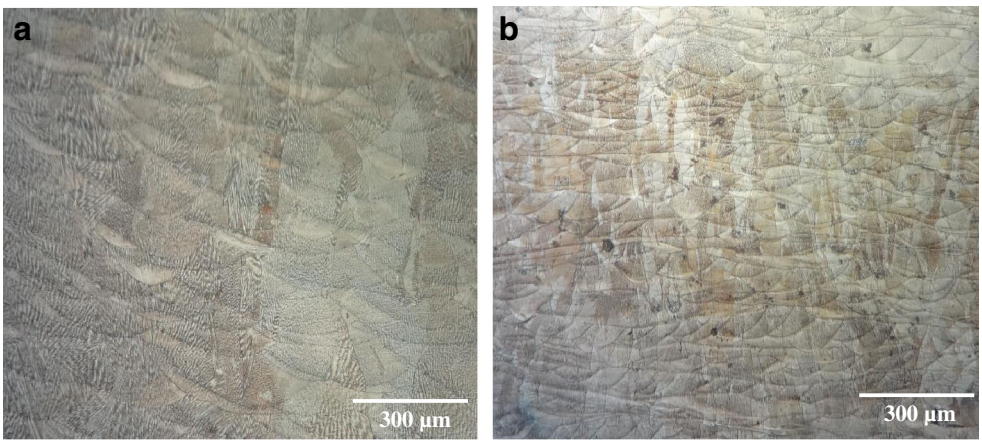


**Fig. 19** The comparative xz plane microstructure of samples, **a** "I-S1000-R30" and **b** "C-S1000-R90"

mechanical properties (hardness and compressive yield strength) significantly decreased.

## 4 Conclusions

In the present study, the samples of IN718 superalloy were prepared by selective laser melting powder bed technique using 4 different scanning strategies (including island scanning with $5 \times 5$ mm$^2$ islands with and without 30° interlayer rotation, and continuous bi-directional scanning with and without 90° interlayer rotation) and 3 different scanning speeds (500, 700, 1000 mm/s). Then, the physical and mechanical properties were characterized. The results showed the following:

- In a given processing parameters, the SLMed samples produced by island strategy obtained a higher density level. Also, the interlayer rotation is a necessary requirement to achieve a dense structure free of aligned pores.
- Increasing the scanning speed leads to a decrease in melt pool width, thermal gradient, powder bed heat input, and an increase in solidification rate, as a result, the formation of the finer cellular microstructure.
- More re-melting and local heat treatment which occurred for depositing layers in "island" strategy would be able to relieve more residual stress of the sample and reduce its hardness and yield strength.

## References


1. Trosch T, Strößner J, Völkl R, Glatzel U (2016) Microstructure and mechanical properties of selective laser melted Inconel 718 compared to forging and casting. Mater Lett 164:428–431
2. Jia Q, Gu D (2014) Selective laser melting additive manufacturing of Inconel 718 superalloy parts: densification, microstructure and properties. J Alloys Compd 585:713–721
3. Valdez M, Kozuch C, Faierson EJ, Jasiuk I (2017) Induced porosity in superalloy 718 through the laser additive manufacturing process: microstructure and mechanical properties. J Alloys Compd 725: 757–764
4. Xia M, Gu D, Yu G, Dai D, Chen H, Shi Q (2017) Porosity evolution and its thermodynamic mechanism of randomly packed powder-bed during selective laser melting of Inconel 718 alloy. Int J Mach Tool Manu 116:96–106
5. Tucho WM, Cuvillier P, Sjolyst-Kverneland A, Hansen V (2017) Microstructure and hardness studies of Inconel 718 manufactured by selective laser melting before and after solution heat treatment. Mater Sci Eng A 689:220–232
6. Deng D, Peng RL, Brodin H, Moverare J (2018) Microstructure and mechanical properties of Inconel 718 produced by selective laser melting: sample orientation dependence and effects of post heat treatments. Mater Sci Eng A 713:294–306
7. Caiazzo F, Alfieri V, Corrado G, Argenio P (2017) Laser powder-bed fusion of Inconel 718 to manufacture turbine blades. Int J Adv Manuf Technol 93:4023–4031
8. Cheng B, Shrestha S, Chou K (2016) Stress and deformation evaluations of scanning strategy effect in selective laser melting. Addit Manuf. https://doi.org/10.1016/j.addma.2016.05.007
9. Wang Z, Guan K, Gao M, Li X, Chen X, Zeng X (2012) The microstructure and mechanical properties of deposited-IN718 by selective laser melting. J Alloys Compd 513:518–523
10. Choi JP, Shin GH, Yang S, Yang DY, Lee JS, Brochu M, Yu JH (2017) Densification and microstructural investigation of Inconel 718 parts fabricated by selective laser melting. Powder Technol 30 C:60–66
11. ASTM B962-15 (2015) Standard Test Methods for Density of Compacted or Sintered Powder Metallurgy (PM) Products Using Archimedes' Principle. ASTM International, West Conshohocken
12. ASTM E9-09 (2009) Standard Test Methods of Compression Testing of Metallic Materials at Room Temperature, West Conshohocken
13. Sames WJ, List FA, Pannala S, Dehoff RR, Babu SS (2016) The metallurgy and processing science of metal additive manufacturing. Int Mater Rev 61(5):315–360
14. Greene GA, Finfrock CC (2001) Oxidation of Inconel 718 in air at high temperatures. Oxid Met 55(5):505–521
15. Takamichi I, Roderick ILG (1993) The physical properties of liquid metals. Clarendon Press, Oxford
16. Guan K, Wang Z, Gao M, Li X, Zeng X (2013) Effects of processing parameters on tensile properties of selective laser melted 304 stainless steel. Mater Des 50:581–586
17. Li R, Shi Y, Liu J, Yao H, Zhang W (2009) Effects of processing parameters on the temperature field of selective laser melting metal powder. Powder Metall Met Ceram 48(3–4):186–195
18. King WE, Barth HD, Castillo VM, Gallegos GF, Gibbs JW, Hahn DE, Kamath C, Rubenchik AM (2014) Observation of keyhole-mode laser melting in laser powder-bed fusion additive manufacturing. J Mater Process Technol 214(12):2915–2925
19. Raghavan S, Zhang B, Wang P, Sun C-N, Nai MLS, Li T, Wei J (2017) Effect of different heat treatments on the microstructure and mechanical properties in selective laser melted Inconel 718 alloy. Mater Manuf Process 32(14):1588–1595
20. Chlebus E, Gruber K, Kuźnicka B, Kurzac J, Kurzynowski T (2015) Effect of heat treatment on the microstructure and mechanical properties of Inconel 718 processed by selective laser melting. Mater Sci Eng A 639(Supplement C):647–655
21. Strößner J, Terock M, Glatzel U (2015) Mechanical and microstructural investigation of nickel-based superalloy IN718 manufactured by selective laser melting (SLM). Adv Eng Mater 17(8):1099–1105
22. Mostafa APR, Brailovski V, Jahazi M, Medraj M (2017) Structure, texture and phases in 3D printed IN718 alloy subjected to homogenization and HIP treatments. Metals 7(6):23